

VIRD: View-Invariant Representation through Dual-Axis Transformation for Cross-View Pose Estimation

Juhye Park¹ Wooju Lee¹ Dasol Hong¹ Changki Sung¹ Youngwoo Seo² Dongwan Kang² Hyun Myung^{1*}

¹Urban Robotics Lab, School of Electrical Engineering, KAIST ²Hanwha Aerospace

¹{jhpark12, dnwn24, ds.hong, cs1032, hmyung}@kaist.ac.kr ²{youngwoo.seo, dongwan.kang}@hanwha.com

Abstract

Accurate global localization is crucial for autonomous driving and robotics, but GNSS-based approaches often degrade due to occlusion and multipath effects. As an emerging alternative, cross-view pose estimation predicts the 3-DoF camera pose corresponding to a ground-view image with respect to a geo-referenced satellite image. However, existing methods struggle to bridge the significant viewpoint gap between the ground and satellite views mainly due to limited spatial correspondences. We propose a novel cross-view pose estimation method that constructs view-invariant representations through dual-axis transformation (VIRD). VIRD first applies a polar transformation to the satellite view to establish horizontal correspondence, then uses context-enhanced positional attention on the ground and polar-transformed satellite features to resolve vertical misalignment, explicitly mitigating the viewpoint gap. A view-reconstruction loss is introduced to strengthen the view invariance further, encouraging the derived representations to reconstruct the original and cross-view images. Experiments on the KITTI and VIGOR datasets demonstrate that VIRD outperforms the state-of-the-art methods without orientation priors, reducing median position and orientation errors by 50.7% and 76.5% on KITTI, and 18.0% and 46.8% on VIGOR, respectively.

1. Introduction

Global localization plays a critical role in autonomous driving and mobile robotics, enabling systems to accurately navigate in real-world environments [8, 19, 25, 36, 37]. Although the global navigation satellite system (GNSS) is widely adopted for outdoor localization [2, 10], its reliability degrades in dense urban areas due to signal occlusion and multipath effects [1, 32, 33].

Cross-view pose estimation (CVPE) has emerged as a promising alternative to GNSS-based localization. It estimates the fine-grained 3 degrees of freedom (DoF) camera

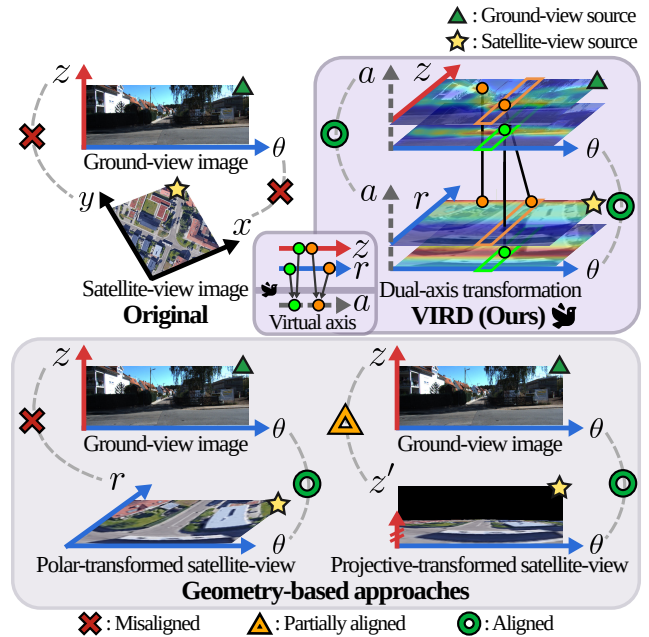


Figure 1. Ground-view and satellite-view images exhibit a large viewpoint gap due to misalignment along both the horizontal and vertical axes on the image plane. Previous geometry-based methods, such as polar and projective transformations, partially mitigated this issue by ensuring horizontal correspondence but could not fully address vertical misalignment. For example, projective transformations often produce severe artifacts around vertical structures such as buildings. VIRD overcomes these limitations through dual-axis transformation, introducing a shared virtual vertical axis a to establish consistent cross-view correspondence.

pose corresponding to a ground-view image by leveraging a geo-referenced satellite image [9, 11, 18, 21, 23, 30, 31, 35]. Early studies often assume coarse orientation priors and refine the pose through iterative optimization within a narrow search space [9, 18, 21, 30]. However, such priors are often inaccurate or unavailable in practice, causing these methods to converge to suboptimal solutions and to suffer from degraded performance. Thus, recent methods have

explored omnidirectional CVPE, which searches the full 360-degree orientation space without requiring orientation priors [11, 16, 35]. To support exhaustive search, these approaches typically extract orientation-aware descriptors from the ground image and match them with satellite descriptors sampled across candidate poses, which improves robustness to local minima [11, 35].

However, existing omnidirectional CVPE methods often neglect the significant viewpoint gap between ground and satellite views, a fundamental challenge for accurate cross-view matching. To address this issue, some methods have adopted content-based cross-attention [11] or contrastive learning [11, 35]. However, these approaches focus primarily on semantic similarity and often ignore spatial correspondences, leaving the viewpoint gap largely unresolved. Geometry-based approaches have also been explored to address this gap through polar [19, 20] and projective transformations [18, 21]. Polar transformations transform the satellite view into ground-aligned horizontal coordinates, but neglect vertical-axis misalignment [19, 20]. Projective transformations, parameterized by camera geometry, aim to simultaneously rectify both horizontal and vertical axes. However, they are highly sensitive to camera calibration errors and prone to severe projection artifacts around vertical structures (*e.g.*, buildings) when depth information is unreliable [18, 21]. Consequently, effectively resolving vertical misalignment remains an open challenge in these geometry-based methods, as qualitatively shown in Fig. 1.

To overcome these limitations, we propose VIRDC (View-Invariant Representation through Dual-axis transformation), a novel omnidirectional CVPE method that effectively bridges the viewpoint gap between ground and satellite views. VIRDC constructs view-invariant descriptors by explicitly transforming cross-view features along horizontal and vertical axes. For the horizontal axis, we apply a polar transformation to the satellite view, following prior works [19, 20]. To resolve the remaining vertical misalignment, we propose context-enhanced positional attention (CEPA), which transforms the ground and polar-transformed satellite features along the vertical axis via positional attention mechanisms [3]. CEPA learns a view-consistent vertical transformation without camera parameters and adaptively captures vertical structures in the ground view by leveraging contextual cues. The view-invariant descriptors are further refined by a view-reconstruction loss that guides the model to reconstruct the original and cross-view images during training.

Our contributions can be summarized as follows:

- A novel omnidirectional CVPE framework constructs view-invariant descriptors to overcome the significant viewpoint gap and enable accurate cross-view matching.
- A dual-axis transformation strategy addresses horizontal and vertical misalignment using polar transformation and

context-enhanced positional attention, reducing reliance on camera parameters.

- A view-reconstruction loss enhances the view invariance of descriptors by training the model to reconstruct the original and cross-view images.
- The proposed method achieved state-of-the-art performance on the KITTI and VIGOR datasets without orientation priors, reducing median position and orientation errors by 50.7% and 76.5% on KITTI, and 18.0% and 46.8% on VIGOR, respectively.

2. Related Works

Limited-angle cross-view pose estimation. Limited-angle cross-view pose estimation estimates the 3-DoF camera pose corresponding to a ground-view image within a geo-referenced satellite image, given a coarse orientation prior. This task was first addressed by Highly-Accurate [18], which refined the pose iteratively using the Levenberg–Marquardt (LM) algorithm [12, 13]. This optimization-based paradigm was later extended using either LM [18, 27–29] or neural pose optimizers [9, 21, 30]. However, these methods remain constrained by their reliance on orientation priors, limiting the search space to a narrow angular range.

Omnidirectional cross-view pose estimation. Omnidirectional cross-view pose estimation eliminates the dependence on orientation priors by estimating the 3-DoF pose across the full 360-degree orientation range [11, 16, 34, 35]. It is often accomplished by matching a ground descriptor with satellite descriptors sampled from candidate poses. In this setting, the descriptors are required to be orientation-aware for accurate orientation estimation and view-invariant to bridge the viewpoint gap. Existing methods often address orientation awareness by leveraging the horizontal azimuthal structure of ground images, while mitigating the viewpoint gap through semantics-based approaches. For example, SliceMatch [11] employs content-based cross-attention, while CCVPE [35] adopts contrastive learning to enhance semantic consistency across views. However, these approaches focus primarily on semantic similarity and fail to explicitly model spatial correspondence between ground and satellite images, which is critical for robust pose estimation. To address this limitation, we propose a novel framework that explicitly models spatial correspondences between ground and satellite views, and incorporates orientation awareness into both ground and satellite descriptors, enabling robust omnidirectional pose estimation.

Geometry-based transformations. Geometry-based transformations have been widely adopted in cross-view pose estimation to reduce the viewpoint gap. Many meth-

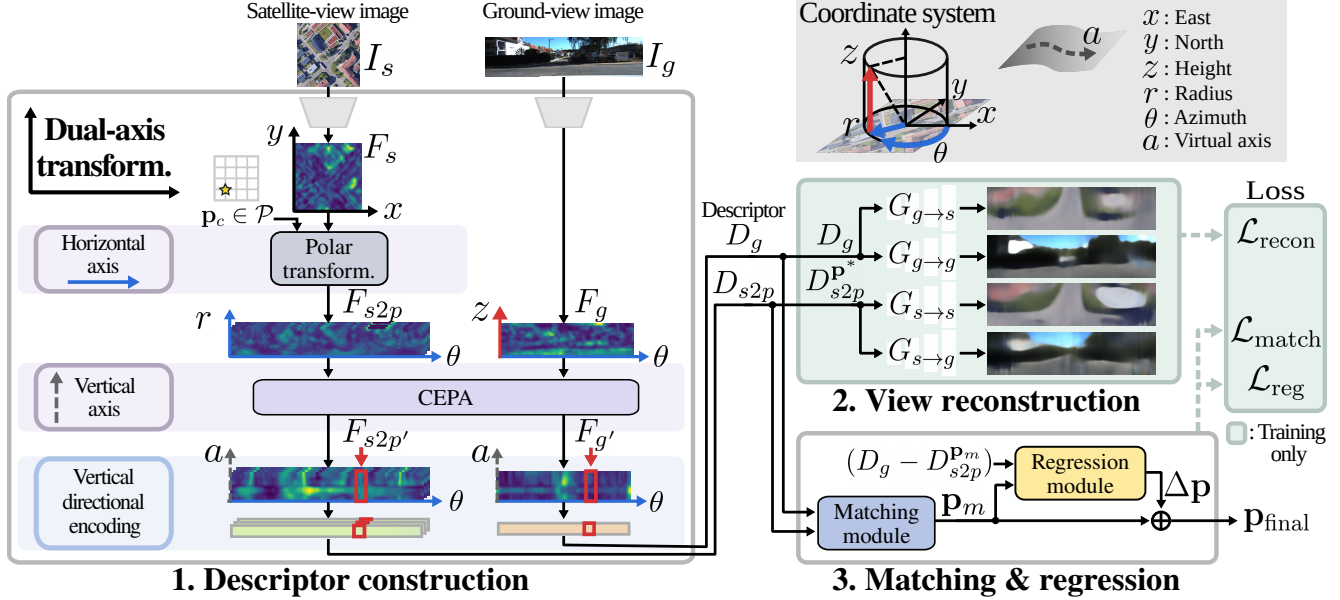


Figure 2. Overview of VIRD. VIRD constructs view-invariant descriptors through dual-axis transformation. The process begins by applying a polar transformation to transform the satellite features F_s into a horizontally corresponding representation to the ground features F_g for each candidate pose $\mathbf{p}_c \in \mathcal{P}$ (the set of candidate poses), generating the polar-transformed features F_{s2p} . The context-enhanced positional attention (CEPA) module then vertically transforms cross-view features through a positional attention mechanism. The resulting satellite and ground features, $F_{s2p'}$ and $F_{g'}$, are compressed along the vertical axis to generate orientation-aware descriptors D_{s2p} and D_g . During training, a view-reconstruction loss is computed at the ground-truth pose \mathbf{p}^* to enforce view invariance by reconstructing both original and cross views. At inference, the final 3-DoF pose is estimated by combining descriptor matching with residual regression.

ods apply polar transformations [19, 20] or projective transformations based on camera parameters [18, 21]. Polar transformations transform the satellite view into a ground-aligned horizontal coordinate but leave vertical misalignment unresolved. In contrast, projective transformations suffer from projection artifacts around vertical structures such as buildings when depth is unavailable. Although recent works incorporate LiDAR data to mitigate these issues [9, 28], such approaches are costly. We therefore propose a novel dual-axis transformation strategy that integrates polar transformation with context-enhanced positional attention, addressing horizontal and vertical misalignment without additional sensors.

3. Proposed Method

Problem definition. Given a ground-view image I_g and a satellite-view image I_s , the goal is to estimate the 3-DoF pose $\mathbf{p} = (x, y, \theta)$ of the ground camera. $(x, y) \in \mathbb{R}^2$ denotes the camera’s position within I_s , where x and y are aligned with east and north, respectively. $\theta \in [-\pi, \pi)$ is the yaw angle measured clockwise from east. The ground image may be either panoramic or a limited horizontal field of view (HFoV), and is assumed to follow a cylindrical projection as in [35]. Following previous works [11, 35], we assume that the camera’s pitch and roll are negligible.

Overview. We propose **VIRD**, a novel cross-view pose estimation method that bridges the viewpoint gap by constructing view-invariant descriptors. As illustrated in Fig. 2, the proposed approach consists of three components: (1) the construction of view-invariant descriptors through dual-axis transformation, followed by vertical directional encoding (Sec. 3.1); (2) a view-reconstruction loss that enhances the view invariance of descriptors by reconstructing both original and cross-view images (Sec. 3.2); and (3) matching and regression modules that predict the final pose (Sec. 3.3). All components are jointly optimized in an end-to-end manner under a unified multi-objective loss function (Sec. 3.4).

3.1. Descriptor construction

Feature extraction. Let $F_g \in \mathbb{R}^{C \times H \times W_g}$ and $F_s \in \mathbb{R}^{C \times A \times A}$ represent features extracted from the ground image I_g and the satellite image I_s using a pretrained convolutional backbone, respectively. Here, C , H , W_g , and A denote the number of channels, the height and width of the ground feature map, and the spatial size of the satellite feature map, respectively. For ground images under cylindrical projection, the horizontal axis of F_g represents azimuthal angles, and the vertical axis corresponds to height. For satellite images, the horizontal axis of F_s represents east and the vertical axis corresponds to north, as illustrated in Fig. 2.

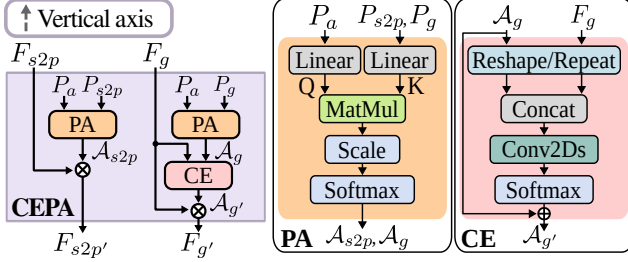


Figure 3. Schematic illustration of the context-enhanced positional attention (CEPA) module consisting of positional attention (PA) and context enhancement (CE). PA generates attention weights \mathcal{A}_g and \mathcal{A}_{s2p} by comparing the shared virtual positional encodings P_a with the positional encodings of the ground and satellite views, P_g and P_{s2p} , respectively. CE then adaptively refines the ground attention weights \mathcal{A}_g using contextual information from the ground feature F_g , resulting in $\mathcal{A}_{g'}$. These attention weights vertically transform the cross views by weighting the features F_g and F_{s2p} with $\mathcal{A}_{g'}$ and \mathcal{A}_{s2p} , respectively.

This inherent misalignment between the coordinate systems of F_g and F_s hinders cross-view matching and full 360-degree orientation search.

Polar transformation. To establish horizontal correspondence between the ground and satellite views, we apply a polar transformation to the satellite feature map F_s , centered at the given candidate position in pixel coordinates (u_c^s, v_c^s) , as in [19, 20]. The transformed feature $F_{s2p}^{(u_c^s, v_c^s)} \in \mathbb{R}^{C \times H \times W_s}$ maps the azimuth and radial distance to the horizontal and vertical axes, respectively, as defined below:

$$\begin{bmatrix} u^s \\ v^s \end{bmatrix} = \begin{bmatrix} u_c^s \\ v_c^s \end{bmatrix} - \rho(v^{s2p}) \begin{bmatrix} \cos\left(\frac{2\pi}{W_s} u^{s2p}\right) \\ \sin\left(\frac{2\pi}{W_s} u^{s2p}\right) \end{bmatrix}, \quad (1)$$

$$\rho(v) := (r_{\max} - r_{\min}) \left(1 - \frac{v}{H}\right) + r_{\min}, \quad (2)$$

where (u^s, v^s) and (u^{s2p}, v^{s2p}) represent the pixel coordinates of the satellite and transformed features, respectively. r_{\min} and r_{\max} denote the minimum and maximum radii of the polar sampling range in pixels. The transformed feature width is $W_s = \frac{2\pi}{\text{HFoV}} \cdot W_g$, ensuring consistency across varying FoVs. This transformation maps the azimuth direction as the horizontal axis of the image plane, assigning an explicit orientation axis to the satellite view and mitigating horizontal misalignment between the cross views.

Positional attention. Although the polar transformation establishes azimuthal correspondence between F_{s2p} and F_g , their vertical axes remain unaligned. As illustrated in Fig. 2, the vertical axis of F_{s2p} corresponds to radial distance, while the vertical axis of F_g represents height. Prior methods [18, 21] address this with projective transformations,

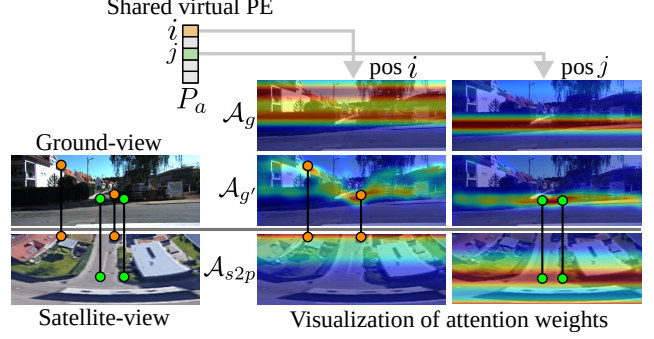


Figure 4. Visualization of attention weights. It shows the activations corresponding to each shared virtual positional encoding (PE). Red indicates stronger activations. Orange and green dots indicate the real spatial correspondence between the views.

but they rely on camera parameters and struggle to handle vertical structures when depth is unavailable. To overcome this, we propose a positional attention mechanism that explicitly learns vertical correspondence within a shared coordinate system, eliminating the dependence on camera parameters, as shown in Fig. 3.

Positional attention computes attention weights from fixed positional encodings and is primarily adopted for its computational efficiency [3, 17]. Here, we reinterpret it as learning a transformation between the vertical coordinates of the ground and satellite views via a shared virtual axis. This axis is defined as a learned, view-invariant vertical coordinate system onto which ground and satellite features are projected. Specifically, we define three positional encodings: shared virtual positional encoding $P_a \in \mathbb{R}^{H_Q \times d_p}$, ground positional encoding $P_g \in \mathbb{R}^{H_K \times d_p}$, and satellite positional encoding $P_{s2p} \in \mathbb{R}^{H_K \times d_p}$. All encodings are sinusoidal encodings of dimension d_p , representing positional information of each vertical image coordinate. H_Q represents the height of the features in the shared coordinate, and $H_K = H$ refers to the height of the features in each view. The positional attention weights $\mathcal{A}_v \in \mathbb{R}^{H_Q \times H_K}$ for each view $v \in \{g, s2p\}$ are computed as:

$$\mathcal{A}_v = \text{Softmax} \left(\frac{(P_a W_v^Q)(P_v W_v^K)^\top}{\sqrt{d_k}} \right), \quad (3)$$

where W_v^Q and W_v^K are the query and key weight matrices for each view, and d_k is the dimension of the queries and keys. These attention weights activate the regions in each view corresponding to the same vertical position in the shared virtual positional space, enabling consistent vertical transformation across horizontal directions. As shown in Fig. 4 (first and third rows), high activations (red) consistently appear along identical road regions and extend to the vertical structures, roughly following the height of building roofs. This learning-based approach allows the model

to capture the floor and the overall vertical layout of the ground view, thereby improving localization accuracy over traditional projective methods.

Context-enhanced positional attention. Although positional attention partially mitigates vertical misalignment based on positional encodings, a key limitation remains: it fundamentally assumes a uniform vertical transformation across all horizontal directions, independent of the input ground context. This assumption facilitates stable learning of cross-view mappings but limits adaptability to vertical structures that vary with horizontal direction and scene context in the ground view. To address this issue, we enhance the ground attention weights \mathcal{A}_g with local ground context. The context-enhanced ground attention weights $\mathcal{A}_{g'} \in \mathbb{R}^{H_Q \times H_K \times W_g}$ are computed as:

$$\mathcal{A}_{g'} = \mathcal{A}_g + \text{Softmax}(\Phi(\mathcal{A}_g \oplus F_g)), \quad (4)$$

where \oplus denotes channel-wise concatenation after shape alignment. The concatenated tensor is processed by convolutional layers Φ , followed by a softmax operation along the H_K dimension. A skip connection facilitates smooth gradient flow. This adjustment enables the model to adaptively transform ground features based on their context, improving vertical correspondence across horizontal directions, as illustrated in Fig. 4 (second row). The pseudocode for this process is provided in the supplementary material.

These attention weights are applied to the features of each view, resulting in vertically transformed features $F_{g'} \in \mathbb{R}^{C \times H_Q \times W_g}$ and $F_{s2p'} \in \mathbb{R}^{C \times H_Q \times W_s}$ as follows:

$$\begin{aligned} F_{g'}[c, h_q, w] &= \sum_{h_k=1}^{H_K} \mathcal{A}_{g'}[h_q, h_k, w] \odot F_g[c, h_k, w], \\ F_{s2p'}[c, h_q, w] &= \sum_{h_k=1}^{H_K} \mathcal{A}_{s2p'}[h_q, h_k, w] \odot F_{s2p}[c, h_k, w], \end{aligned} \quad (5)$$

where \odot denotes element-wise multiplication.

Vertical directional encoding. The 3D features transformed along the horizontal and vertical axes, $F_{g'}$ and $F_{s2p'}$, are compressed along the vertical direction using shared multi-layer perceptrons (MLPs) applied to each column. The resulting features are then flattened across the channel and width dimensions, while preserving the width information, following [35]. This process yields orientation-aware 1D descriptors, $D_g \in \mathbb{R}^{K_g}$ and $D_{s2p} \in \mathbb{R}^{K_s}$, with $K_s = \frac{2\pi}{\text{HFoV}} \cdot K_g$.

3.2. View-reconstruction

To enhance view invariance, we introduce a view-reconstruction loss that trains each descriptor to reconstruct both the original and cross views. This loss encourages the model to learn a view-invariant representation that captures shared structures between cross views.

Reconstruction mechanism. Given the ground-truth pose $\mathbf{p}^* = (x^*, y^*, \theta^*)$, the satellite descriptor $D_{s2p}^{(x^*, y^*)}$ obtained in Sec. 3.1 is horizontally shifted by θ^* and cropped to match the ground descriptor, yielding $D_{s2p}^{\mathbf{p}^*} \in \mathbb{R}^{K_g}$. The aligned descriptors are reshaped and vertically expanded via MLP layers, then processed by 2D convolutional and up-sampling layers to reconstruct the target view. Each decoder $G_{i \rightarrow j}$ generates a full-resolution image of the target view j from the descriptor of the source view i .

Reconstruction loss. The view-reconstruction loss is defined using the ℓ_1 -loss as follows:

$$\begin{aligned} \mathcal{L}_{\text{origin}} &= \|I_g - G_{g \rightarrow g}(D_g)\|_1 + \|I_{s2p}^{\mathbf{p}^*} - G_{s \rightarrow s}(D_{s2p}^{\mathbf{p}^*})\|_1, \\ \mathcal{L}_{\text{cross}} &= \|I_g - G_{s \rightarrow g}(D_{s2p}^{\mathbf{p}^*})\|_1 + \|I_{s2p}^{\mathbf{p}^*} - G_{g \rightarrow s}(D_g)\|_1, \\ \mathcal{L}_{\text{recon}} &= \alpha_1 \mathcal{L}_{\text{origin}} + \alpha_2 \mathcal{L}_{\text{cross}}, \end{aligned} \quad (6)$$

where \mathbf{p}^* is the ground-truth pose, and α_1, α_2 are weighting coefficients. The polar-transformed satellite image $I_{s2p}^{\mathbf{p}^*}$ is generated following the same alignment procedure as that of $D_{s2p}^{\mathbf{p}^*}$. This loss guides the descriptors to better encode vertical structures, where the viewpoint gap is particularly large, and thus helps resolve ambiguities in visually similar road scenes.

3.3. Matching and regression

Descriptor matching. To estimate the coarse pose, the ground descriptor is matched with satellite descriptors from candidate poses $\mathbf{p}_c = (x_c, y_c, \theta_c)$, sampled from a predefined spatial grid. The similarity score for each candidate pose, $S^{\mathbf{p}_c}$, is computed using the cosine similarity between D_g and $D_{s2p}^{\mathbf{p}_c}$. To train discriminative descriptors, we adopt the InfoNCE loss [14], which encourages high similarity at the ground-truth pose \mathbf{p}^* and penalizes other non-matching poses. During inference, the candidate pose that maximizes $S^{\mathbf{p}_c}$ is selected as the coarse matching pose \mathbf{p}_m .

Pose regression. The regression module refines the matching pose \mathbf{p}_m by predicting residuals $\Delta \mathbf{p} = (\Delta x, \Delta y, \Delta \theta)$ to compensate for the resolution limits of descriptor matching. The residuals are predicted from the difference between D_g and $D_{s2p}^{\mathbf{p}_m}$, together with \mathbf{p}_m , and are added to produce the final pose $\mathbf{p}_{\text{final}} = \mathbf{p}_m + \Delta \mathbf{p}$. It is trained using the ℓ_2 -loss computed over the pose residuals.

3.4. Training details

Total loss. The final objective combines the view-reconstruction, matching, and regression losses as $\mathcal{L} = \mathcal{L}_{\text{recon}} + \mathcal{L}_{\text{match}} + \mathcal{L}_{\text{reg}}$. Detailed formulations of $\mathcal{L}_{\text{match}}$ and \mathcal{L}_{reg} are provided in the supplementary material.

Table 1. Position and orientation estimation errors on the KITTI [5] dataset without orientation priors. Lon. and Med. are abbreviations for longitudinal and median, respectively. * denotes results reproduced from the official implementations. Best in **bold**, second best underlined.

Method	Backbone	Area	Position						Orientation			
			Error (m) ↓		Lateral recall (%) ↑		Lon. recall (%) ↑		Error (°) ↓		Recall (%) ↑	
			Mean	Med.	R@1m	R@5m	R@1m	R@5m	Mean	Med.	R@1°	R@5°
HighlyAccurate [18]	VGG16	Same	15.51	15.97	5.17	25.44	4.66	25.39	89.91	90.75	0.61	2.89
SliceMatch [11]	VGG16	Same	9.39	5.41	39.73	87.92	13.63	49.22	8.71	4.42	11.35	55.82
CCVPE [35]	EfficientNet-B0	Same	6.88	3.47	53.30	85.13	25.84	68.49	15.01	6.12	8.96	42.75
DenseFlow* [23]	ResNet18 [6]	Same	6.47	4.26	73.87	97.27	14.82	58.50	3.72	<u>0.99</u>	<u>50.62</u>	90.06
FG2* [31]	DINOv2 [15]	Same	5.81	4.26	24.97	75.78	24.57	<u>75.14</u>	89.64	90.26	0.42	2.73
VIRD (Ours)	VGG16	Same	5.47	2.07	<u>79.46</u>	<u>98.30</u>	31.65	75.78	5.16	1.02	<u>49.32</u>	92.95
VIRD (Ours)	EfficientNet-B0	Same	<u>5.55</u>	<u>2.22</u>	79.43	98.41	29.84	73.89	<u>4.87</u>	0.98	51.2	<u>92.82</u>
HighlyAccurate [18]	VGG16	Cross	15.50	16.02	5.60	25.60	5.64	25.76	89.84	89.85	0.60	2.65
SliceMatch [11]	VGG16	Cross	14.85	11.85	24.00	72.89	7.17	33.12	<u>23.64</u>	7.96	31.69	31.69
CCVPE [35]	EfficientNet-B0	Cross	13.94	10.98	23.42	60.46	11.81	42.12	77.84	63.84	3.14	14.56
DenseFlow* [23]	ResNet18	Cross	25.85	18.84	19.80	47.15	4.35	23.75	69.51	42.04	10.87	29.57
FG2* [31]	DINOv2	Cross	13.58	11.72	9.92	42.48	10.95	43.03	90.12	90.42	0.65	2.93
VIRD (Ours)	VGG16	Cross	<u>12.30</u>	<u>7.05</u>	<u>43.61</u>	<u>81.86</u>	<u>12.88</u>	<u>46.83</u>	25.10	<u>2.22</u>	27.65	<u>69.86</u>
VIRD (Ours)	EfficientNet-B0	Cross	11.12	5.41	45.88	85.49	14.97	52.55	22.03	1.87	<u>30.39</u>	74.87

4. Experiments

4.1. Datasets

KITTI dataset. KITTI [5] contains forward-facing ground-view images captured by a vehicle in Karlsruhe, Germany, covering urban, rural, and highway scenes. Following [18], each ground image is paired with a 100 m × 100 m satellite patch at 0.20 m/pixel resolution, with the camera assumed to be located within the central 40 m × 40 m region. To simulate a realistic scenario without an orientation prior, we introduce a random orientation sampled uniformly from $[-\pi, \pi)$, following [11, 35].

VIGOR dataset. VIGOR [38] consists of ground-view panoramas and corresponding satellite images from four U.S. cities. Each satellite image covers a 70 m × 70 m area. Ground panoramas are aligned so their vertical center corresponds to the north in satellite images. A satellite patch is labeled as positive if the ground camera lies within its central quarter region. Otherwise, it is semi-positive. We use only positive pairs, following [11, 35]. The same-area and cross-area splits are adopted from [38], with corrected labels following [11]. We evaluate the model under both known and unknown orientations, following [11, 35].

4.2. Evaluation metrics

We adopt the evaluation metrics from [11], reporting mean and median errors for position (in meters) and orientation (in degrees) across all datasets. For KITTI, we additionally compute recall following [11, 35], defined as the percentage of predictions within 1 m and 5 m in both lateral and longitudinal directions, and within 1° and 5° in orientation.

4.3. Implementation details

Consistent with SliceMatch [11] and CCVPE [35], we use a VGG16 [22] and an EfficientNet-B0 [24] backbone pre-trained on ImageNet [4]. Candidate poses are sampled on a uniform grid over the satellite image. For KITTI, we use a 5 × 5 grid during training and 20 × 20 at test time. For VIGOR, the grid is 7 × 7 for training and 25 × 25 for testing. The sampling stride determines the number of orientation candidates, with 16 candidates during training for both datasets, and 70 for KITTI and 80 for VIGOR in testing. Training is performed for 10 epochs on an NVIDIA RTX A5000 GPU using the Adam optimizer [7], with a learning rate of 10^{-4} and a batch size of 4. Further details are provided in the supplementary material.

4.4. Comparison with state-of-the-art methods

KITTI dataset. Tab. 1 compares the proposed method with the state-of-the-art methods on the KITTI dataset for VGG16 and EfficientNet-B0 backbones. Our method consistently outperformed all baselines in both same-area and cross-area settings, demonstrating its effectiveness in omnidirectional cross-view pose estimation. With EfficientNet-B0, it reduced the median position and orientation errors by 50.7% and 76.5% in the cross-area setting.

These superior results stem from VIRD’s ability to explicitly bridge the viewpoint gap and integrate a robust coarse-to-fine pose estimation framework. Existing approaches suffer from inherent limitations in either representation or architecture. Geometry-based methods using projective transformations [18, 23] and semantics-based methods [11, 35] often leave spatial misalignment unresolved, thereby degrading pose estimation accuracy. HighlyAccurate [18], an iterative optimization-based framework with a narrow search range, tends to converge to suboptimal solu-

Table 2. Position and orientation estimation errors on the VIGOR [38] dataset. ‘Aligned’ refers to the case where the ground image orientation is known. For unaligned images, the models estimate the full 360-degree. † indicates the use of a two-step inference specific to the method in [31] to boost performance. Best in **bold**, second best underlined.

Method	Backbone	Aligned	Same-Area				Cross-Area			
			Position (m) ↓		Orientation (°) ↓		Position (m) ↓		Orientation (°) ↓	
			Mean	Median	Mean	Median	Mean	Median	Mean	Median
MCC [34]	VGG16	✓	6.94	3.64	-	-	9.05	5.14	-	-
SliceMatch [11]	VGG16	✓	5.18	2.58	-	-	5.53	2.55	-	-
CCVPE [35]	EfficientNet-B0	✓	3.60	1.36	-	-	4.97	1.68	-	-
DenseFlow [23]	ResNet18	✓	3.03	0.97	-	-	5.01	2.42	-	-
HC-Net [30]	EfficientNet-B0	✓	2.65	1.17	-	-	<u>3.35</u>	1.59	-	-
FG2 [31]	DINOv2	✓	1.95	<u>1.08</u>	-	-	2.41	1.37	-	-
VIRD (Ours)	VGG16	✓	3.14	1.39	-	-	4.83	1.77	-	-
VIRD (Ours)	EfficientNet-B0	✓	<u>2.57</u>	1.14	-	-	3.85	<u>1.47</u>	-	-
MCC [34]	VGG16	×	9.87	6.25	56.86	16.02	12.66	9.55	72.13	29.97
SliceMatch [11]	VGG16	×	8.41	5.07	28.43	5.15	8.48	5.64	26.20	5.18
CCVPE [35]	EfficientNet-B0	×	3.74	<u>1.42</u>	12.83	6.62	<u>5.41</u>	<u>1.89</u>	27.78	13.58
DenseFlow [23]	ResNet18	×	4.97	1.90	<u>11.20</u>	1.59	7.67	3.67	<u>17.63</u>	2.94
FG2 [31]	DINOv2	×	8.95	7.32	15.02	2.94	10.02	8.14	31.41	5.45
FG2† [31]	DINOv2	×	3.78	1.70	12.63	1.44	5.95	2.40	28.41	2.20
VIRD (Ours)	VGG16	×	<u>3.71</u>	1.52	12.45	<u>1.21</u>	6.05	1.95	24.55	<u>1.56</u>
VIRD (Ours)	EfficientNet-B0	×	3.00	1.20	9.52	0.96	4.61	1.55	16.50	1.17

Table 3. Ablation study of dual-axis transformation on KITTI [5].

	Pos. error (m) ↓		Orien. error (°) ↓	
	Mean	Med.	Mean	Med.
Projective (S2G)	14.37	10.59	37.92	3.84
Projective (G2S)	17.10	15.20	47.62	5.44
Polar	15.26	11.75	39.92	4.00
Polar + PA (Ours)	13.92	9.76	35.17	3.44
Polar + CEPA (Ours)	13.83	8.88	31.35	3.36

tions under unreliable orientation priors. Global descriptor-based methods such as SliceMatch [11] remain limited by coarse matching accuracy. Even FG2 [31], which leverages height-aware 3D point selection to mitigate the viewpoint gap, degrades in orientation estimation due to its sparse point matching mechanism. In contrast, VIRD jointly resolves horizontal and vertical misalignment through dual-axis transformation and refines poses via a fine-grained regression after coarse global matching, achieving stable convergence and superior accuracy across metrics.

VIGOR dataset. Tab. 2 presents the evaluation results on the VIGOR dataset. With the EfficientNet-B0 backbone, our method reduced median position and orientation errors by 18.0% and 46.8% under the unaligned and cross-area settings, demonstrating strong generalization ability for pose estimation. Although FG2 [31] performs well in the aligned setting by leveraging 3D structural information via point matching, its accuracy drops sharply in the unaligned setting due to sparse point correspondences. This limitation reduces scalability in real-world environments where reliable orientation priors are often unavailable. To alleviate this issue, FG2 introduces a two-step variant (denoted as FG2†

Table 4. Ablation study of model components on KITTI [5].

	Pos. error (m) ↓		Orien. error (°) ↓	
	Mean	Med.	Mean	Med.
Polar + CEPA	13.83	8.88	31.35	3.36
+ $\mathcal{L}_{\text{origin}}$	13.34	8.29	28.26	3.31
+ $\mathcal{L}_{\text{cross}}$	12.84	8.10	26.30	3.21
+ $\mathcal{L}_{\text{origin}} + \mathcal{L}_{\text{cross}}$	12.72	7.90	21.91	3.05
+ $\mathcal{L}_{\text{origin}} + \mathcal{L}_{\text{cross}} + \mathcal{L}_{\text{reg}}$	12.30	7.05	25.10	2.22

in Tab. 2) that sequentially estimates orientation and refines pose, yet it still underperforms compared with VIRD.

4.5. Ablation study

All ablations were conducted on the KITTI dataset using a VGG16 backbone in the cross-area evaluation setting.

Dual-axis transformation. As shown in Tab. 3, we evaluated the effectiveness of dual-axis transformation. The baselines include satellite-to-ground projective transformation [18] (S2G), ground-to-satellite projective transformation [21] (G2S), and polar transformation without attention (Polar). Incorporating positional attention (Polar + PA) outperformed all baselines, achieving median errors of 9.76 m and 3.44° for position and orientation, respectively. Adding contextual information (Polar + CEPA) further reduced the median position error to 8.88 m. These results highlight that the dual-axis transformation is a powerful alternative to traditional geometry-based approaches. Fig. 5 (second column) visualizes CEPA’s attention weights, demonstrating its ability to capture vertical correspondences between structures in the ground view (e.g., roofs, roads) and the corresponding vertical positions in the satellite view.

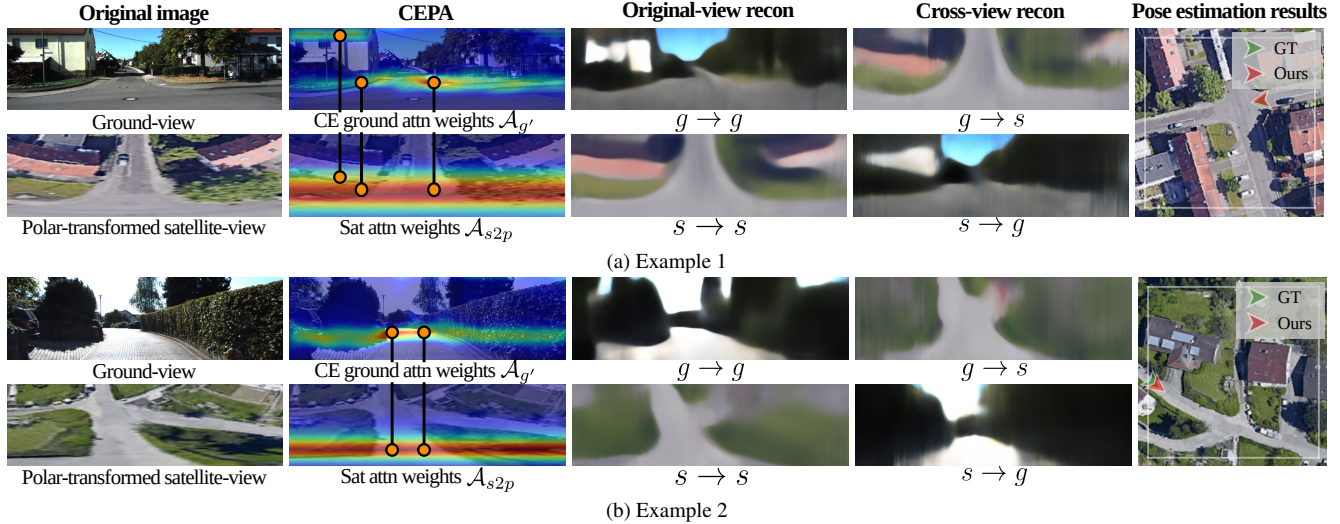


Figure 5. Visualization of CEPA’s attention weights, view reconstruction, and pose estimation results from VIRID.

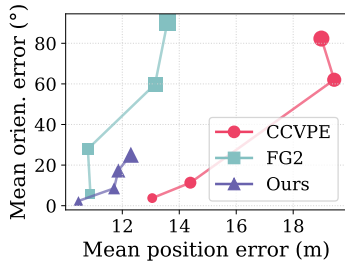


Figure 6. Ablation study of robustness to orientation noise on KITTI [5]. Larger markers denote higher noise levels ($\pm 10^\circ$, $\pm 60^\circ$, $\pm 120^\circ$, and $\pm 180^\circ$).

View-reconstruction loss. Tab. 4 evaluates the impact of the view-reconstruction loss. Incorporating both original and cross-view reconstruction consistently improves performance compared with CEPA without reconstruction. The most notable improvement is a 39.1% reduction in mean orientation error when applying both reconstruction losses. This result highlights the importance of capturing vertical structures, particularly in ambiguous scenarios where similar road shapes can lead to reversed orientation predictions. As illustrated in the third and fourth columns of Fig. 5, the trained descriptors successfully reconstruct road layouts and approximate building shapes while filtering out objects not shared across views such as cars and side roads. These findings demonstrate that the view-reconstruction loss promotes view-invariant representations by encouraging the model to focus on cross-view consistent structures.

Regression module. The regression module refines the predicted coarse pose to improve pose estimation precision.

As shown in Tab. 4, it reduces the median position and orientation errors by 0.85 m and 0.83° , respectively, compared with the model without regression. Although the regression module slightly increases the mean orientation error, this effect arises from higher directional precision: when coarse matching predicts the opposite direction, the refined orientation becomes farther from the ground truth, while predictions close to the correct direction become more precise.

Robustness to orientation noise. Fig. 6 shows the mean position and orientation errors of CCVPE [35], FG2 [31], and our VIRID under different levels of orientation noise ($\pm 10^\circ$, $\pm 60^\circ$, $\pm 120^\circ$, and $\pm 180^\circ$). Because orientation noise simultaneously affects both position and orientation estimates, we jointly visualize them to capture their coupled behavior. As orientation noise increases, the errors become larger, and greater distances between markers indicate more severe performance degradation. VIRID consistently maintains low errors across all noise levels, demonstrating strong robustness to orientation noise compared with CCVPE and FG2.

5. Conclusion

This paper presented VIRID, a novel cross-view pose estimation method that bridges the ground–satellite viewpoint gap by constructing view-invariant representations. To ensure view invariance, VIRID introduces a dual-axis transformation and a view-reconstruction loss. Experiments on the KITTI and VIGOR datasets demonstrate the superiority of the proposed method. Future work will extend this approach to more challenging 6-DoF pose estimation tasks for both on the ground and airborne.

References

- [1] Boaz Ben-Moshe, Elazar Elkin, Harel Levi, and Ayal Weissman. Improving accuracy of GNSS devices in urban canyons. In *Proceedings of the Canadian Conference on Computational Geometry*, pages 511–515, 2011. 1
- [2] Benjamin Congram and Timothy D Barfoot. Relatively lazy: Indoor-outdoor navigation using vision and GNSS. In *Proceedings of the Conference on Computer and Robot Vision*, pages 25–32, 2021. 1
- [3] Artur Back de Luca, George Giapitzakis, Shenghao Yang, Petar Veličković, and Kimon Fountoulakis. Positional attention: Out-of-distribution generalization and expressivity for neural algorithmic reasoning. *arXiv preprint arXiv:2410.01686*, 2024. 2, 4
- [4] Jia Deng, Wei Dong, Richard Socher, Li-Jia Li, Kai Li, and Li Fei-Fei. ImageNet: A large-scale hierarchical image database. In *Proceedings of the IEEE/CVF Conference on Computer Vision and Pattern Recognition*, pages 248–255, 2009. 6
- [5] Andreas Geiger, Philip Lenz, Christoph Stiller, and Raquel Urtasun. Vision meets robotics: The KITTI dataset. *The International Journal of Robotics Research*, 32(11):1231–1237, 2013. 6, 7, 8, 1, 2, 3, 4
- [6] Kaiming He, Xiangyu Zhang, Shaoqing Ren, and Jian Sun. Deep residual learning for image recognition. In *Proceedings of the IEEE/CVF Conference on Computer Vision and Pattern Recognition*, pages 770–778, 2016. 6
- [7] Diederik Kingma and Jimmy Ba. ADAM: A method for stochastic optimization. In *Proceedings of the International Conference on Learning Representations*, 2015. 6
- [8] Alex Junho Lee, Seungwon Song, Hyungtae Lim, Woojoon Lee, and Hyun Myung. (LC)²: LiDAR-camera loop constraints for cross-modal place recognition. *IEEE Robotics and Automation Letters*, 8(6):3589–3596, 2023. 1
- [9] Wooju Lee, Juhye Park, Dasol Hong, Changki Sung, Youngwoo Seo, Dongwan Kang, and Hyun Myung. PIDLoc: Cross-view pose optimization network inspired by PID Controllers. *arXiv preprint arXiv:2503.02388*, 2025. 1, 2, 3
- [10] Mathias Lemmens and Mathias Lemmens. Global navigation satellite systems and inertial navigation. *Geo-information: Technologies, Applications and the Environment*, pages 55–83, 2011. 1
- [11] Ted Lentsch, Zimin Xia, Holger Caesar, and Julian FP Kooij. SliceMatch: Geometry-guided aggregation for cross-view pose estimation. In *Proceedings of the IEEE/CVF Conference on Computer Vision and Pattern Recognition*, pages 17225–17234, 2023. 1, 2, 3, 6, 7, 5
- [12] Kenneth Levenberg. A method for the solution of certain non-linear problems in least squares. *Quarterly of Applied Mathematics*, 2(2):164–168, 1944. 2
- [13] Donald W Marquardt. An algorithm for least-squares estimation of nonlinear parameters. *Journal of the Society for Industrial and Applied Mathematics*, 11(2):431–441, 1963. 2
- [14] Aaron van den Oord, Yazhe Li, and Oriol Vinyals. Representation learning with contrastive predictive coding. *arXiv preprint arXiv:1807.03748*, 2018. 5, 3
- [15] Maxime Oquab, Timothée Darcet, Théo Moutakanni, Huy Vo, Marc Szafraniec, Vasil Khalidov, Pierre Fernandez, Daniel Haziza, Francisco Massa, Alaaeldin El-Nouby, et al. DINOv2: Learning robust visual features without supervision. *Transactions on Machine Learning Research*, 2024. 6
- [16] Paul-Edouard Sarlin, Daniel DeTone, Tsun-Yi Yang, Armen Avetisyan, Julian Straub, Tomasz Malisiewicz, Samuel Rota Buló, Richard Newcombe, Peter Kotschieder, and Vasileios Balntas. OrienterNet: Visual localization in 2D public maps with neural matching. In *Proceedings of the IEEE/CVF Conference on Computer Vision and Pattern Recognition*, pages 21632–21642, 2023. 2
- [17] Felix Schmidt and Mattia A Di Gangi. Bridging the gap between position-based and content-based self-attention for neural machine translation. In *Proceedings of the Eighth Conference on Machine Translation*, pages 507–521, 2023. 4, 1
- [18] Yujiao Shi and Hongdong Li. Beyond cross-view image retrieval: Highly accurate vehicle localization using satellite image. In *Proceedings of the IEEE/CVF Conference on Computer Vision and Pattern Recognition*, pages 17010–17020, 2022. 1, 2, 3, 4, 6, 7
- [19] Yujiao Shi, Liu Liu, Xin Yu, and Hongdong Li. Spatial-aware feature aggregation for cross-view image based geolocalization. *Advances in Neural Information Processing Systems*, pages 10090–10100, 2019. 1, 2, 3, 4
- [20] Yujiao Shi, Xin Yu, Dylan Campbell, and Hongdong Li. Where am I looking at? Joint location and orientation estimation by cross-view matching. In *Proceedings of the IEEE/CVF Conference on Computer Vision and Pattern Recognition*, pages 4064–4072, 2020. 2, 3, 4
- [21] Yujiao Shi, Fei Wu, Akhil Perincherry, Ankit Vora, and Hongdong Li. Boosting 3-DoF ground-to-satellite camera localization accuracy via geometry-guided cross-view transformer. In *Proceedings of the IEEE/CVF International Conference on Computer Vision*, pages 21516–21526, 2023. 1, 2, 3, 4, 7
- [22] Karen Simonyan and Andrew Zisserman. Very deep convolutional networks for large-scale image recognition. *arXiv preprint arXiv:1409.1556*, 2014. 6
- [23] Zhenbo Song, Xianghui Ze, Jianfeng Lu, and Yujiao Shi. Learning dense flow field for highly-accurate cross-view camera localization. *Advances in Neural Information Processing Systems*, 36:70612–70625, 2023. 1, 6, 7
- [24] Mingxing Tan and Quoc Le. EfficientNet: Rethinking model scaling for convolutional neural networks. In *Proceedings of the International Conference on Machine Learning*, pages 6105–6114, 2019. 6
- [25] Sebastian Thrun, Wolfram Burgard, and Dieter Fox. *Probabilistic Robotics*. MIT Press, 2005. 1
- [26] Ashish Vaswani, Noam Shazeer, Niki Parmar, Jakob Uszkoreit, Llion Jones, Aidan N Gomez, Lukasz Kaiser, and Illia Polosukhin. Attention is all you need. *Advances in Neural Information Processing Systems*, 30, 2017. 1
- [27] Shan Wang, Yanhao Zhang, Akhil Perincherry, Ankit Vora, and Hongdong Li. View consistent purification for accurate cross-view localization. In *Proceedings of the IEEE/CVF*

- International Conference on Computer Vision*, pages 8197–8206, 2023. [2](#)
- [28] Shan Wang, Yanhao Zhang, Ankit Vora, Akhil Perincherry, and Hongdong Li. Satellite image based cross-view localization for autonomous vehicle. In *Proceedings of the IEEE International Conference on Robotics and Automation*, pages 3592–3599, 2023. [3](#)
- [29] Shan Wang, Chuong Nguyen, Jiawei Liu, Yanhao Zhang, Sundaram Muthu, Fahira Afzal Maken, Kaihao Zhang, and Hongdong Li. View from above: Orthogonal-view aware cross-view localization. In *Proceedings of the IEEE/CVF Conference on Computer Vision and Pattern Recognition*, pages 14843–14852, 2024. [2](#)
- [30] Xiaolong Wang, Runsen Xu, Zhuofan Cui, Zeyu Wan, and Yu Zhang. Fine-grained cross-view geo-localization using a correlation-aware homography estimator. *Advances in Neural Information Processing Systems*, 36:5301–5319, 2023. [1](#), [2](#), [7](#)
- [31] Zimin Xia and Alexandre Alahi. FG²: Fine-grained cross-view localization by fine-grained feature matching. In *Proceedings of the IEEE/CVF Conference on Computer Vision and Pattern Recognition*, pages 6362–6372, 2025. [1](#), [6](#), [7](#), [8](#)
- [32] Zimin Xia, Olaf Booij, Marco Manfredi, and Julian FP Kooij. Geographically local representation learning with a spatial prior for visual localization. In *Proceedings of the European Conference on Computer Vision Workshops*, pages 557–573, 2020. [1](#)
- [33] Zimin Xia, Olaf Booij, Marco Manfredi, and Julian FP Kooij. Cross-view matching for vehicle localization by learning geographically local representations. *IEEE Robotics and Automation Letters*, 6(3):5921–5928, 2021. [1](#)
- [34] Zimin Xia, Olaf Booij, Marco Manfredi, and Julian FP Kooij. Visual cross-view metric localization with dense uncertainty estimates. In *Proceedings of the European Conference on Computer Vision*, pages 90–106, 2022. [2](#), [7](#)
- [35] Zimin Xia, Olaf Booij, and Julian FP Kooij. Convolutional cross-view pose estimation. *IEEE Transactions on Pattern Analysis and Machine Intelligence*, 2023. [1](#), [2](#), [3](#), [5](#), [6](#), [7](#), [8](#), [4](#)
- [36] Hongji Yang, Xiufan Lu, and Yingying Zhu. Cross-view geo-localization with layer-to-layer transformer. *Advances in Neural Information Processing Systems*, 34:29009–29020, 2021. [1](#)
- [37] Huan Yin, Xuecheng Xu, Sha Lu, Xieyuanli Chen, Rong Xiong, Shaojie Shen, Cyrill Stachniss, and Yue Wang. A survey on global LiDAR localization: Challenges, advances and open problems. *International Journal of Computer Vision*, 132(8):3139–3171, 2024. [1](#)
- [38] Sijie Zhu, Taojiannan Yang, and Chen Chen. VIGOR: Cross-view image geo-localization beyond one-to-one retrieval. In *Proceedings of the IEEE/CVF Conference on Computer Vision and Pattern Recognition*, pages 3640–3649, 2021. [6](#), [7](#), [3](#)

VIRD: View-Invariant Representation through Dual-Axis Transformation for Cross-View Pose Estimation

Supplementary Material

Table of Contents

A Context-Enhanced Positional Attention	1
B View-Reconstruction Loss	2
C Matching and Regression Modules	3
D Additional Implementation Details	3
E Applicability to Pinhole Camera Models	4
F Additional Ablation Studies	4
G Error Statistics across Random Seeds	5
H Computational Resources and Runtime	5
I. Extra Qualitative Results	6
J. Societal Impact	6
K Limitations	6

Unless otherwise specified, all experiments are conducted on the KITTI [5] dataset under the cross-area setting.

A. Context-Enhanced Positional Attention

A.1. Pseudocode

Algorithm 1 Pseudocode for CEPA

```

1: Input:
2:   Query positional encoding  $P_a$  #  $(H_Q, d_p)$ 
3:   Key positional encoding  $P_v$  #  $(H_K, d_p)$ 
4:   Ground attention weights  $A_g$  #  $(H_Q, H_K)$ 
5:   Ground feature  $F_g$  #  $(B, C, H_K, W_g)$ 
6: Output:
7:   Positional attention weights  $A_v$  #  $(H_Q, H_K)$ 
8:   Context-enhanced attention weights  $A_{g'}$  #  $(B, H_Q, H_K, W_g)$ 
9: function CAL_POSITIONAL_ATTENTION_WEIGHTS( $P_a, P_v$ )
10:   $Q \leftarrow \text{linear\_projection}(P_a)$ 
11:   $K \leftarrow \text{linear\_projection}(P_v)$ 
12:   $A_v \leftarrow (QK^T) / \sqrt{d_k}$ 
13:   $A_v \leftarrow \text{softmax}(A_v, \text{dim} = -1)$ 
14:  return  $A_v$ 
15: end function
16: function CONTEXT_ENHANCEMENT( $A_g, F_g$ )
17:   $A_g' \leftarrow \text{reshape}(A_g, 1, H_Q, 1, H_K, 1)$ 
18:   $A_g' \leftarrow \text{repeat}(A_g', B, 1, 1, 1, W_g)$  #  $(B, H_Q, 1, H_K, W_g)$ 
19:
20:   $F_g' \leftarrow \text{reshape}(F_g, B, 1, C, H_K, W_g)$ 
21:   $F_g' \leftarrow \text{repeat}(F_g', 1, H_Q, 1, 1, 1)$  #  $(B, H_Q, C, H_K, W_g)$ 
22:
23:   $\text{feat} \leftarrow \text{concat}(A_g', F_g', \text{dim} = 2)$  #  $(B, H_Q, C+1, H_K, W_g)$ 
24:   $\text{feat} \leftarrow \text{reshape}(\text{feat}, B \cdot H_Q, C+1, H_K, W_g)$ 
25:   $\text{feat} \leftarrow \text{conv2d}(\text{feat})$  #  $(B \cdot H_Q, 1, H_K, W_g)$ 
26:   $\text{feat} \leftarrow \text{reshape}(\text{feat}, B, H_Q, H_K, W_g)$ 
27:   $\hat{A} \leftarrow \text{softmax}(\text{feat}, \text{dim} = -2)$ 
28:   $A_{g'} \leftarrow \hat{A} + A_g'$  # after broadcasting
29:  return  $A_{g'}$ 
30: end function

```

Algorithm 2 Pseudocode for vertical feature transformation

```

1: Input:
2:   Shared virtual positional encoding  $P_a$  #  $(H_Q, d_p)$ 
3:   Ground positional encoding  $P_g$  #  $(H_K, d_p)$ 
4:   Satellite positional encoding  $P_{s2p}$  #  $(H_K, d_p)$ 
5:   Ground feature  $F_g$  #  $(B, C, H_K, W_g)$ 
6:   Polar-transformed satellite feature  $F_{s2p}$  #  $(B, C, H_K, W_s)$ 
7: Output:
8:   Vertically-transformed ground feature  $F_{g'}$  #  $(B, C, H_Q, W_g)$ 
9:   Vertically-transformed satellite feature  $F_{s2p'}$  #  $(B, C, H_Q, W_s)$ 
10: function VERTICAL_TRANSFORM( $P_a, P_g, P_{s2p}, F_g, F_{s2p}$ )
11:   $A_g \leftarrow \text{CAL\_POSITIONAL\_ATTN\_WEIGHTS}(P_a, P_g)$ 
12:   $A_{s2p} \leftarrow \text{CAL\_POSITIONAL\_ATTN\_WEIGHTS}(P_a, P_{s2p})$ 
13:   $A_{g'} \leftarrow \text{CONTEXT\_ENHANCEMENT}(A_g, F_g)$ 
14:   $F_{g'}[b, c, h_q, w] \leftarrow \sum_k A_{g'}[b, h_q, h_k, w] F_g[b, c, h_k, w]$ 
15:   $F_{s2p'}[b, c, h_q, w] \leftarrow \sum_k A_{s2p}[h_q, h_k] F_{s2p}[b, c, h_k, w]$ 
16:  return  $F_{g'}, F_{s2p'}$ 
17: end function

```

A.2. CEPA vs. content-based attention

Fig. A compares the proposed context-enhanced positional attention (CEPA) with a content-based attention (CBA) baseline. CBA follows the conventional formulation in which attention weights are computed directly from input content, such as image features [17]. We implement CBA using the self- and cross-attention layers from Slice-Match [11] and apply them with a polar transformation (Polar + CBA). CBA yields a moderate gain in the same-area setting, where training and test scenes share similar visual patterns. However, its performance degrades in the cross-area setting. Because CBA derives attention weights from image content, it overfits to scene-specific semantics and fails to capture the spatial correspondence across unseen environments. In contrast, CEPA consistently achieves superior performance in both same- and cross-area evaluations. It first derives attention weights from positional cues and then refines them using ground context, allowing the model to more effectively focus on spatial correspondence rather than appearance. These results demonstrate that explicitly modeling positional correspondence is crucial for robust cross-view pose estimation.

A.3. Positional encoding types

Tab. A compares different types of positional encodings, including sinusoidal, sinusoidal-learnable, learnable, and 2D sinusoidal variants. The sinusoidal encoding is fixed and follows the formulation of [26]. The sinusoidal-learnable variant applies a nonlinear projection to the fixed sinusoidal encoding. In contrast, the learnable encoding is initialized as a fully trainable tensor without relying on any predefined

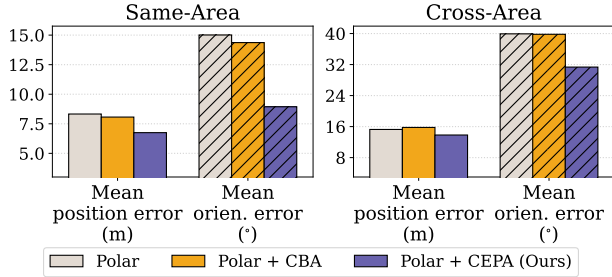


Figure A. Comparison of content-based attention (CBA) and context-enhanced positional attention (CEPA) on KITTI [5].

Table A. Positional attention performance with various positional encoding variants on KITTI [5].

	Pos. error (m) ↓		Orien. error (°) ↓	
	Mean	Med.	Mean	Med.
Sinusoidal pe	13.92	9.76	35.17	3.44
Sinusoidal learnable pe	14.28	10.63	33.82	3.41
Learnable pe	15.23	12.06	36.23	4.04
2D sinusoidal pe	14.68	10.31	33.57	3.57

positional pattern. The 2D sinusoidal variant extends positional information to both horizontal and vertical directions in the ground view.

Among these variants, the fixed 1D sinusoidal encoding (Polar + PA in the main paper’s Tab. 3) achieves the best overall performance, showing the lowest position error and competitive orientation accuracy. These results indicate that vertical transformations across views can be learned more reliably when positional encodings are fixed and 1D. Notably, the comparison with the 2D sinusoidal variant suggests that encoding both horizontal and vertical positional information may introduce ambiguity in establishing spatial correspondence. This may occur because the standard positional attention mechanism relies solely on positional information, which might not adequately account for the complexity of vertical structures in ground-view images. In contrast, assuming a consistent vertical transformation along the horizontal direction provides a more stable inductive bias that facilitates reliable spatial correspondence. This finding further highlights the strength of the proposed CEPA, which uses fixed 1D positional encoding to model shared vertical transformation while adaptively capturing horizontal variations in the ground view through context enhancement.

B. View-Reconstruction Loss

B.1. Effect of view-reconstruction on CEPA

This section analyzes how the view-reconstruction loss influences the learning of CEPA. During training, the view-reconstruction loss encourages the ground and satellite de-

Table B. Comparison of different reconstruction loss types on KITTI [5].

	Pos. error (m) ↓		Orien. error (°) ↓	
	Mean	Med.	Mean	Med.
ℓ_1	12.72	7.90	21.91	3.05
ℓ_2	13.14	8.30	25.74	3.31
SSIM	12.92	8.00	25.23	3.34
Percep	14.00	9.78	29.55	3.31

scriptors to reconstruct both their original and cross views. This supervision enables the descriptors to embed structural cues more effectively, not only from regions with small viewpoint gaps, such as road surfaces, but also from structures with large viewpoint gaps, including tall buildings and other vertically dominant elements. By promoting the preservation of meaningful information even in these challenging regions, the view-reconstruction loss allows CEPA to attend more effectively to vertical structures and ultimately learn more stable vertical transformations between the cross views. As shown in Fig. B, the visualization of the context-enhanced ground attention weights highlights this effect. In example (a), CEPA with the view-reconstruction loss exhibits stronger activations around roof regions, indicating improved vertical correspondence. In example (b), the model successfully captures the overpass structure that is missed when the view-reconstruction loss is removed.

B.2. Reconstruction loss types

Several loss functions for view reconstruction are evaluated, including ℓ_1 , ℓ_2 , SSIM, and perceptual loss, as summarized in Tab. B. Among them, the ℓ_1 loss achieves the best performance, yielding a mean position error of 12.72 m and a mean orientation error of 21.91°.

The goal of view reconstruction in our framework is not to generate perceptually realistic images, but to provide stable structural supervision that promotes view-invariant descriptors. ℓ_2 loss is less suitable because it strongly penalizes large pixel differences that naturally arise between ground and satellite views, leading to unstable gradients. SSIM focuses on luminance and contrast consistency, which are not reliably shared across cross views, thereby weakening the geometric cues needed for spatial correspondence. Perceptual loss is also ineffective: it compares high-level semantic features extracted by networks trained on perspective natural images, but such semantics differ substantially between ground and satellite views, producing inconsistent gradients that degrade geometric structure. In contrast, the ℓ_1 loss provides uniformly weighted, geometry-preserving supervision that avoids overfitting to appearance or semantics. This property makes the ℓ_1 loss the most stable and effective choice for enforcing view invariance in cross-view matching.

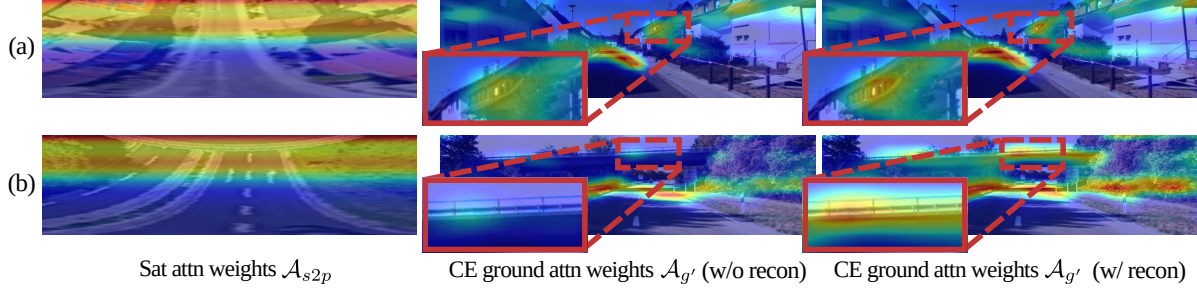


Figure B. Effect of the view-reconstruction loss on CEPA. The first row presents example (a), and the second row presents example (b). For each example, the satellite attention \mathcal{A}_{s2p} and the context-enhanced ground attention $\mathcal{A}_{g'}$ are visualized at the same vertical position in the shared virtual positional encoding space. The view-reconstruction loss stabilizes the learning of vertical transformations in CEPA, yielding stronger roof activations in example (a) and successful detection of overpass structures in example (b). Regions with stronger activations are highlighted in red.

C. Matching and Regression Modules

C.1. Shifting and cropping of satellite descriptor

Given a candidate pose $\mathbf{p}_c = (x_c, y_c, \theta_c)$, a satellite descriptor $D_{s2p}^{(x_c, y_c)} \in \mathbb{R}^{K_s}$ is constructed via dual-axis transformation and vertical directional encoding. This descriptor is initially aligned such that its central vertical line corresponds to the east, i.e., $\theta = 0$. To align it with the orientation θ_c , the descriptor is cyclically shifted along the horizontal axis by $\frac{\theta_c}{2\pi} \cdot W_s$, following prior work [35]. After alignment, the descriptor is center-cropped to match the size of the ground descriptor $D_g \in \mathbb{R}^{K_g}$, yielding the orientation-aligned satellite descriptor $D_{s2p}^{\mathbf{p}_c} \in \mathbb{R}^{K_g}$. Similarly, the polar-transformed satellite image $I_{s2p}^{\mathbf{p}_c}$, which is used in the view-reconstruction loss, is shifted and cropped in the same manner to ensure spatial alignment with I_g .

C.2. Regression network architecture

The regression module first reshapes the 1D descriptor difference into a 2D representation with channel and width dimensions, then passes it through a series of 1D convolutional layers to obtain a high-dimensional embedding. The resulting feature is flattened and concatenated with the coarse pose. MLPs are applied to predict the pose residual $\Delta \mathbf{p} = (\Delta x, \Delta y, \Delta \theta)$ relative to the ground truth. The predicted output is scaled to operate within a predefined search range.

C.3. Training details

Matching loss. To train discriminative descriptors, we adopt the InfoNCE loss [14], encouraging high similarity at the ground-truth pose \mathbf{p}^* and penalizing n -th non-matching pose \mathbf{p}_n , following [11, 35]:

$$\mathcal{L}_{\text{match}} = -\log \left(\frac{\exp(S^{\mathbf{p}^*} / \tau)}{\sum_{n=1}^N \exp(S^{\mathbf{p}_n} / \tau) + \exp(S^{\mathbf{p}^*} / \tau)} \right), \quad (7)$$

where $S^{\mathbf{p}^*}$ and $S^{\mathbf{p}_n}$ are similarity scores at the ground-truth pose and the n -th non-matching pose among N samples, respectively. τ is a temperature scaling parameter.

Regression loss. The regression module is trained using the ℓ_2 -loss computed over pose residuals:

$$\mathcal{L}_{\text{reg}} = \beta (\|\Delta x - \Delta x^*\|_2 + \|\Delta y - \Delta y^*\|_2 + \|\Delta \theta - \Delta \theta^*\|_2), \quad (8)$$

where $(\Delta x^*, \Delta y^*, \Delta \theta^*)$ denote the ground-truth pose residuals, and β is a weighting coefficient.

Regression training. To train the regression module, N_r coarse poses are randomly sampled around the ground-truth pose within predefined spatial and angular ranges, where reliable refinement is feasible. For each sampled pose \mathbf{p}_r , the satellite descriptor $D_{s2p}^{\mathbf{p}_r}$ is computed using the same shift-and-crop mechanism described in Sec. C.1. The regression loss for each sampled pose is computed as described in Eq. (8), and the final loss is obtained by averaging over all N_r samples.

D. Additional Implementation Details

We provide additional implementation details in Sec. 4.3. The spatial size of I_g is 256×1024 for KITTI and 320×640 for VIGOR, and I_s is 512×512 for both datasets. The temperature parameter τ is set to 0.05. The loss coefficients α_1 , α_2 , and β are set to 1, 10, and 5, respectively. The polar transform is configured with r_{\min} and r_{\max} set to 6 m and 40 m for KITTI [5], and to 0 m and 30 m for VIGOR [38], respectively. For the CEPA module, the shared virtual axis height H_Q is set equal to the ground feature height H , which is 16 and 20 for KITTI and VIGOR, respectively. To improve computational efficiency, the number of channels is reduced by a factor of four after feature extraction with the VGG16 backbone. The feature extractor weights are shared when using the VGG16 backbone; in all other

Table C. Impact of cylindrical projection on pinhole camera on KITTI [5].

Cylindrical projection	Pos. error (m) ↓		Orien. error (°) ↓	
	Mean	Med.	Mean	Med.
×	15.26	11.75	39.92	4.00
✓	15.10	11.62	38.97	4.13

Table D. Ablation study of the temperature parameter on KITTI [5].

τ	Pos. error (m) ↓		Orien. error (°) ↓	
	Mean	Med.	Mean	Med.
0.1	16.09	13.21	38.54	4.34
0.05	15.26	11.75	39.92	4.00
0.01	17.18	14.93	53.59	6.17

settings, weights are not shared. Zero-padding is used as the default setting. For panorama images, circular padding is applied along the horizontal axis. For regression, the search range is limited to ± 4 m, ± 4 m, and $\pm 3.6^\circ$ in x , y , and θ dimensions, respectively.

E. Applicability to Pinhole Camera Models

Following prior work [35], we assume a cylindrical projection for all cameras. This assumption is not strictly valid for pinhole cameras, meaning that the polar-transformed satellite image does not perfectly correspond to the horizontal axis of a pinhole image. Despite this mismatch, the polar transformation remains effective for reducing the viewpoint gap. As shown in Tab. C, models trained with raw pinhole images and those trained with a cylindrical projection applied to the same images yield nearly identical performance. This result indicates that the projection mismatch has negligible influence on accuracy, demonstrating that VIRD can be applied to pinhole cameras without difficulty.

F. Additional Ablation Studies

F.1. Hyperparameters

Temperature The temperature parameter τ is evaluated using a baseline model that includes only the polar transformation, excluding the proposed attention and reconstruction modules. Tab. D shows that the best performance is achieved at 0.05.

Loss coefficients Tab. E presents the results of ablation experiments on the loss coefficients. The best performance is achieved when the loss coefficients for original-view reconstruction (α_1), cross-view reconstruction (α_2), and regression (β) are set to 1, 10, and 5, respectively. The matching loss coefficient is set to its default value of 1, and thus no ablation was performed for this parameter.

Table E. Ablation study of the loss coefficients on KITTI [5].

α_1	α_2	β	Pos. error (m) ↓		Orien. error (°) ↓	
			Mean	Med.	Mean	Med.
0.1	0	0	13.43	8.54	30.08	3.30
1	0	0	13.34	8.29	28.26	3.31
5	0	0	13.90	9.04	27.01	3.34
1	5	0	12.61	7.64	25.72	3.16
1	10	0	12.72	7.90	21.91	3.05
1	20	0	13.25	8.39	24.13	3.54
1	10	1	12.45	7.48	23.59	2.47
1	10	5	12.30	7.05	25.10	2.22

Table F. Ablation study of the regression search range on KITTI [5].

Range	Area	Lat. (%) ↑	Lon. (%) ↑	Orien. (%) ↑
		R@1m	R@1m	R@1°
± 2 m, ± 2 m, $\pm 1.8^\circ$	Same	79.30	29.21	44.16
± 4 m, ± 4 m, $\pm 3.6^\circ$	Same	79.46	31.65	49.32
± 6 m, ± 6 m, $\pm 4.8^\circ$	Same	74.77	28.49	51.63
± 2 m, ± 2 m, $\pm 1.8^\circ$	Cross	44.37	12.98	26.81
± 4 m, ± 4 m, $\pm 3.6^\circ$	Cross	43.61	12.88	27.65
± 6 m, ± 6 m, $\pm 4.8^\circ$	Cross	40.20	12.11	27.06

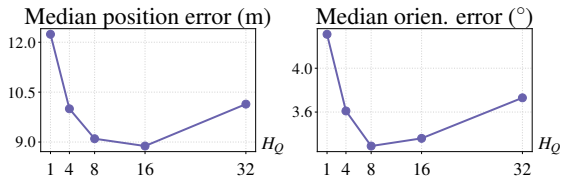


Figure C. Ablation study of H_Q on KITTI [5].

Regression search range Tab. F reports the effect of varying the search range for the regression module. The model achieves high average recall accuracy when the search range is limited to ± 4 m in translation and $\pm 3.6^\circ$ in orientation. This setting performs comparably to the tighter configuration of ± 2 m and $\pm 1.8^\circ$, while significantly outperforming broader ranges such as ± 6 m. These results demonstrate that the optimal search range for the regression module lies within a moderate range, where it can more precisely focus on local feature differences and more effectively correct residual pose errors.

F.2. Impact of shared virtual axis height

As shown in Fig. C, we conduct an ablation study on the height of the shared virtual axis H_Q , which defines the resolution of the shared coordinate system in the CEPA module. Performance peaks around $H_Q = 16$, demonstrating that this resolution is sufficient to capture vertical correspondences between cross views. Notably, performance drops markedly at $H_Q = 1$, where vertical information is simply collapsed into a single dimension without establishing vertical correspondence. This result supports the necessity of the

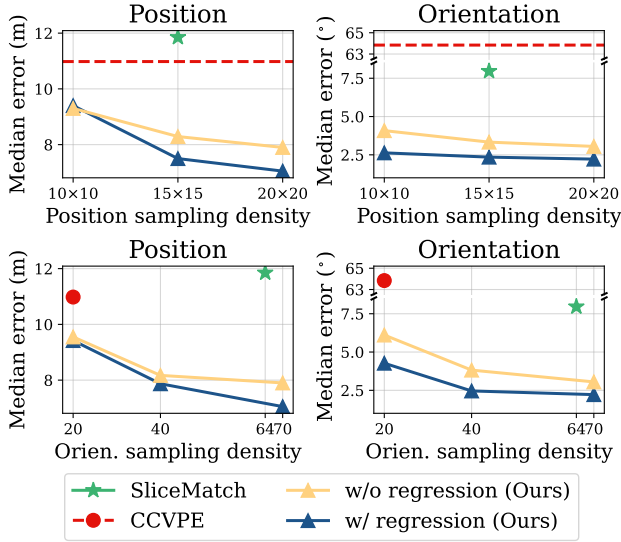


Figure D. Ablation study of candidate pose sampling density, compared with SliceMatch [11] and CCVPE [35]. For the proposed method, the number of orientation candidates is fixed to 70 during position sampling, and the position grid size is fixed to 20×20 during orientation sampling. SliceMatch performs matching only on $15 \times 15 \times 64$ candidate poses. For CCVPE, position prediction is performed at the original resolution, while orientation prediction first matches 20 candidates and then performs regression. Because CCVPE is independent of the number of position samples, its performance is shown as a horizontal line.

shared virtual axis for resolving vertical misalignment. On the other hand, increasing H_Q to 32 leads to degraded performance, suggesting that excessively high resolution may introduce redundancy that hinders stable learning.

F.3. Effect of candidate pose sampling density

An ablation study is conducted to examine the impact of candidate pose sampling density, with the analysis separated into position and orientation sampling. For position sampling, three spatial resolutions are compared: 10×10 , 15×15 , and 20×20 . For orientation sampling, four candidate counts are evaluated: 20, 40, 64, and 70. These sampling configurations are selected with reference to prior works [11, 35].

Fig. D shows that increasing the number of candidate poses leads to reduced median errors in both position and orientation. This trend highlights the benefit of finer sampling resolution. Although denser sampling improves accuracy, it also increases computational cost. Sec. H.2 examines this trade-off in more detail. We also compare two global descriptor-based approaches: SliceMatch [11] and CCVPE [35]. The proposed method consistently improves over all baselines across the tested sampling densities, demonstrating the superiority of our approach.

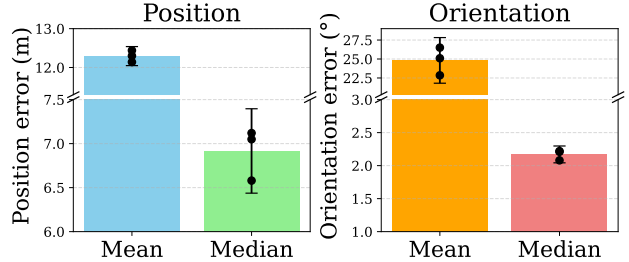


Figure E. Error statistics across five random seeds for the proposed method. Error bars indicate $\pm 2\sigma$ standard deviations, computed from five independent runs.

G. Error Statistics across Random Seeds

To assess the robustness of the proposed method, performance variation is reported across the five independent runs using different random seeds. Fig. E visualizes the mean and median errors for both position and orientation, providing a statistical perspective on the results presented in Tab. 1. Error bars represent $\pm 2\sigma$ standard deviations, computed as the sample standard deviation across five independent runs. This captures variability due to random initialization and training dynamics. While the normality assumption is not formally tested due to the limited number of samples, the visualization provides a practical view of the method’s stability across repeated runs.

H. Computational Resources and Runtime

H.1. Training and inference

We report the computational cost during both training and inference. All experiments were conducted on a local workstation equipped with an RTX A5000 GPU with 24 GB of memory. A batch size of 4 was used during training and 1 during inference. During training, the peak GPU memory usage reached approximately 24 GB on both the KITTI and VIGOR datasets. Using the VGG16 backbone, training required about 15 hours on KITTI and 38 hours on VIGOR.

Tab. G summarizes GPU memory usage and runtime during inference on the KITTI dataset. With the VGG16 backbone and a sampling density of $20 \times 20 \times 70$, VIRD requires 9.0 GB of GPU memory and achieves 12 frames per second (FPS). Using EfficientNet-B0 yields similar memory usage while slightly improving runtime to 13 FPS. Compared with prior methods, the proposed approach offers substantially higher accuracy while maintaining comparable memory usage and fast inference speed. These results demonstrate that VIRD is computationally efficient and practical for real-world deployment.

Table G. Inference memory usage and runtime of the proposed method and prior approaches on the KITTI [5] dataset, including the impact of different sampling densities. Sampling density is defined as the number of candidate poses, computed as the product of position and orientation sampling sizes. All results are measured using the official implementations on an RTX A5000 GPU with 24 GB memory.

Method	Backbone	Sampling density	Med. position error	Med. orientation error	GPU memory usage (GB)	Inference runtime (FPS)
HighlyAccurate [18]	VGG16	-	16.02	89.85	7.1	3
CCVPE [35]	EfficientNet-B0	-	10.98	63.84	5.2	20
DenseFlow [23]	ResNet18	-	18.84	42.04	6.4	9
FG2 [31]	DINOv2	-	11.72	90.42	3.5	6
VIRD (Ours)	VGG16	10×10×70	9.40	2.63	4.8	27
VIRD (Ours)	VGG16	15×15×70	7.50	2.35	6.6	18
VIRD (Ours)	VGG16	20×20×70	7.05	2.22	9.0	12
VIRD (Ours)	EfficientNet-B0	20×20×70	5.41	1.87	9.0	13

H.2. Trade-off between sampling density and efficiency

Tab. G also illustrates how increasing the candidate pose sampling density affects computational cost. Higher sampling densities lead to increased memory usage and longer inference times, reflecting a clear trade-off between accuracy and efficiency. Therefore, users may refer to Tab. G to select a sampling configuration that best meets their performance and runtime constraints.

I. Extra Qualitative Results

I.1. Attention weights visualization

We provide additional qualitative examples of attention weights. Fig. F visualizes \mathcal{A}_g , $\mathcal{A}_{g'}$, and \mathcal{A}_{s2p} , which are computed by applying context-enhanced positional attention to ground and polar-transformed satellite features. The positional attention weights \mathcal{A}_g and \mathcal{A}_{s2p} , which are computed without context enhancement, exhibit consistent patterns along the horizontal direction due to learning a shared vertical transformation. In contrast, the context-enhanced attention $\mathcal{A}_{g'}$ adaptively incorporates contextual information for each horizontal position, resulting in more diverse horizontal attention distributions. Overall, these visualizations indicate that the proposed approach effectively captures meaningful spatial correspondence between ground and satellite views.

I.2. Reconstructed images visualization

We present additional qualitative examples of reconstructed images. Fig. G visualizes the reconstruction results of the ground and satellite descriptors in both original and cross views. The reconstructed outputs recover road layouts and capture coarse building structures, while naturally suppressing view-specific elements such as vehicles and side roads. These observations indicate that the view-reconstruction loss effectively drives the descriptors toward view-invariant representations that are consistently preserved across ground and satellite views.

J. Societal Impact

The proposed method advances cross-view localization by enabling accurate ground-to-satellite matching in GNSS-denied environments, such as dense urban areas, where satellite imagery is available. This functionality supports critical applications, including autonomous navigation and disaster response. However, it raises potential privacy concerns and risks of unintended uses, such as surveillance or location-based profiling. These concerns highlight the importance of considering ethical deployment practices and conducting privacy assessments in downstream applications.

K. Limitations

A key limitation of the proposed method is its dependence on the number of candidate poses sampled during inference. Since both model accuracy and computational efficiency are sensitive to the sampling resolution, the method requires manual tuning of the sampling density to meet application-specific constraints, which limits its scalability in practice. In addition, similar to most existing cross-view pose estimation approaches, our method assumes that roll and pitch angles can be neglected. Although this assumption holds in relatively flat urban environments, it may lead to significant errors in challenging terrains such as mountainous regions or areas with strong elevation variations. To address these limitations, future work could focus on reducing the method’s reliance on candidate pose sampling resolution and extending the approach toward estimating the full 6-DoF pose without assuming fixed roll and pitch.

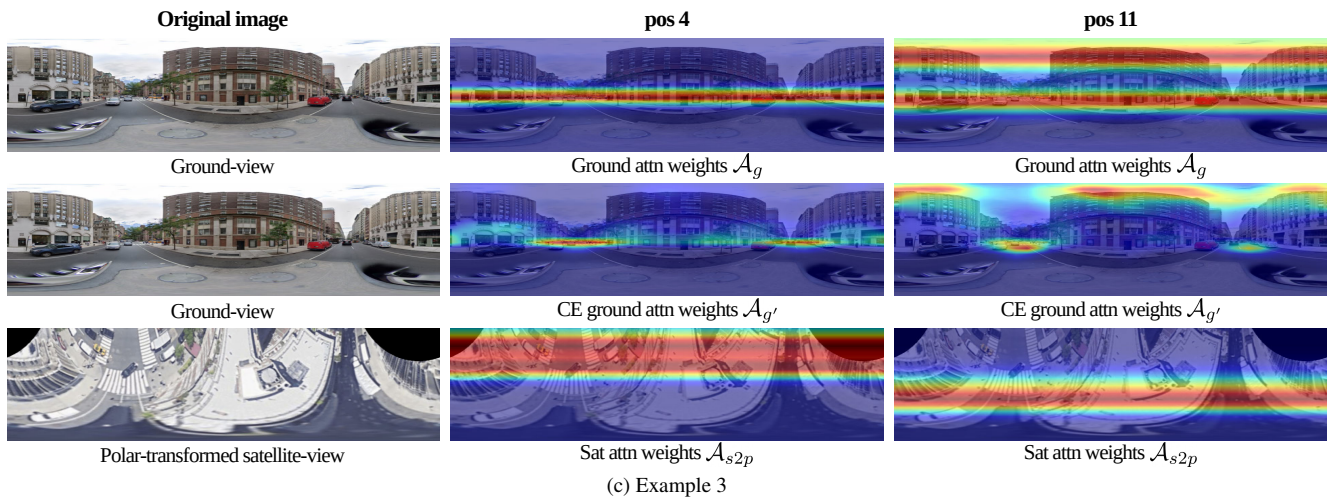
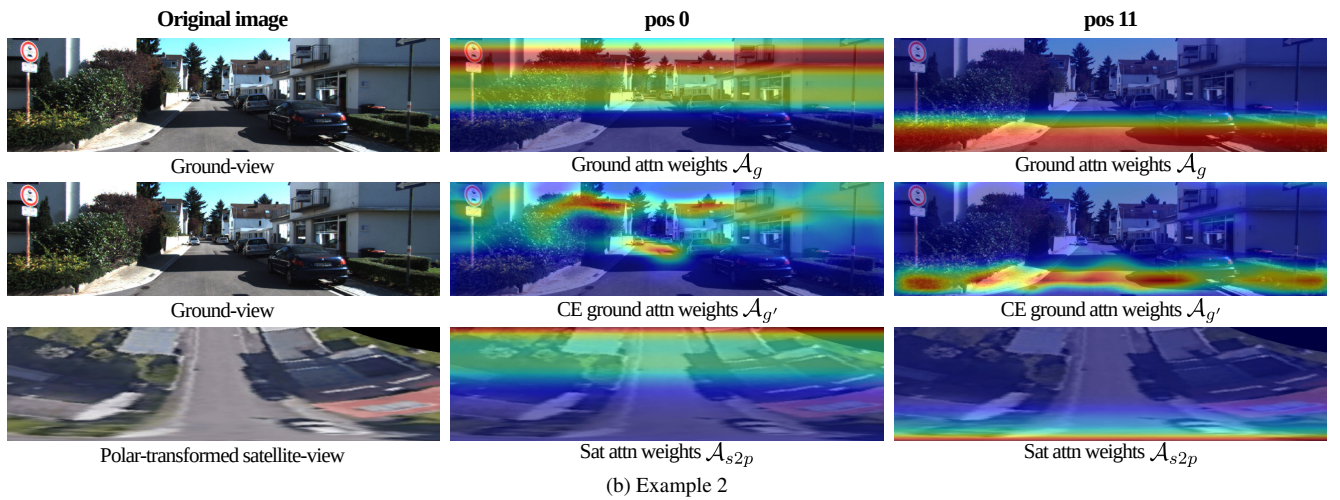
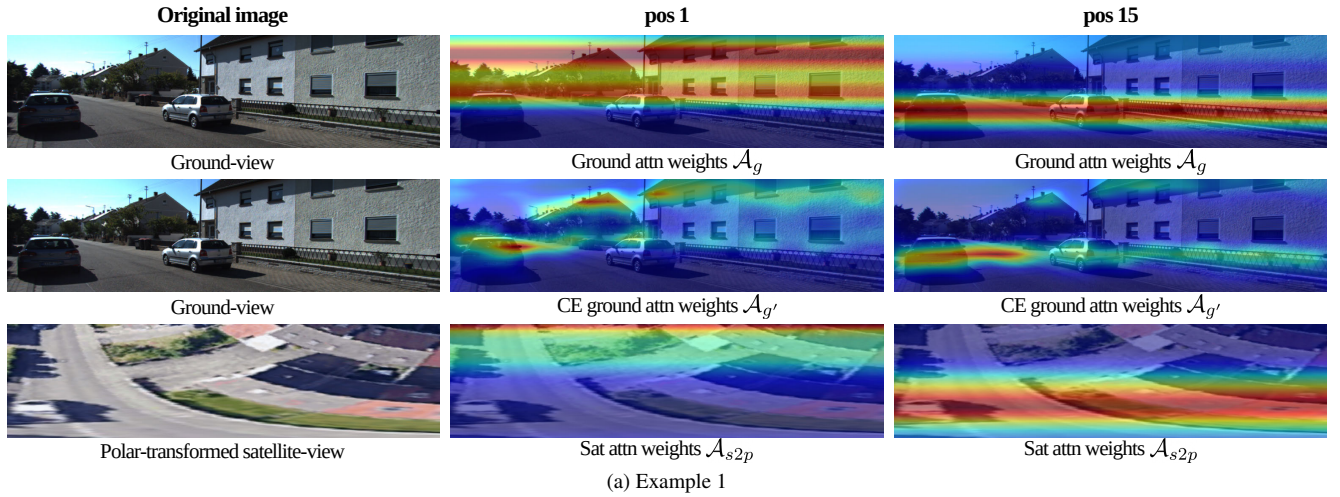


Figure F. Visualization of the attention weights \mathcal{A}_g , $\mathcal{A}_{g'}$, and \mathcal{A}_{s2p} at selected positions in the shared virtual positional encoding space. CE and pos denote the context-enhanced attention and the positions in the shared virtual positional encoding space, respectively. Regions with stronger activations are highlighted in red.

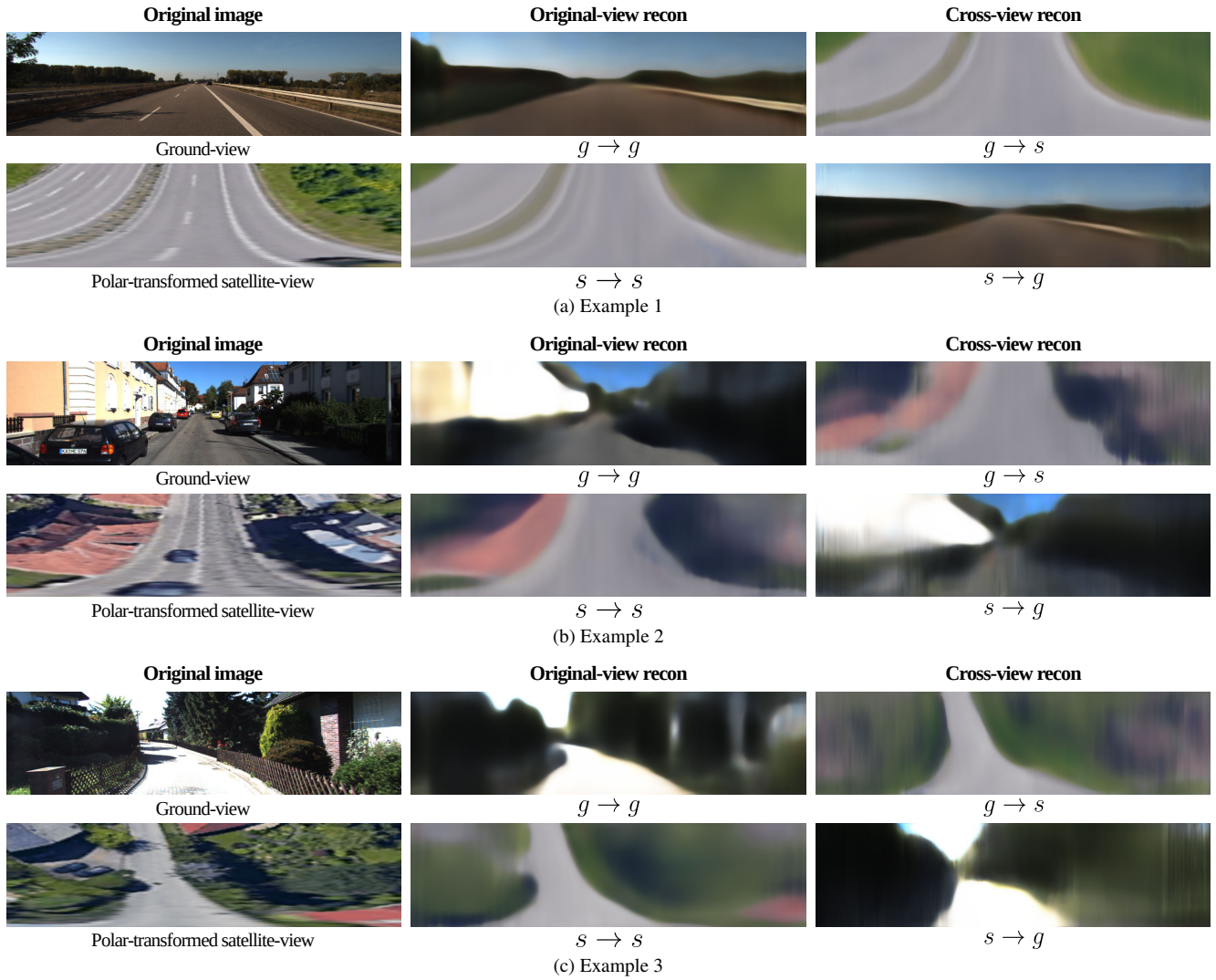


Figure G. Visualization of reconstructed images from ground and satellite descriptors in both original and cross views. Each subfigure is denoted as $i \rightarrow j$, where $i, j \in \{s, g\}$ indicate the source and target views, respectively. The pairs $g \rightarrow g$ and $s \rightarrow s$ indicate original-view reconstructions, whereas $g \rightarrow s$ and $s \rightarrow g$ represent cross-view reconstructions.